Numerical simulation of undrained insertion problems in geotechnical engineering with the Particle Finite Element Method (PFEM)

Lluís Monforte [a,*], Marcos Arroyo [a], Josep Maria Carbonell [b], Antonio Gens [a]

[a] Department of Geotechnical Engineering, Universitat Politècnica de Catalunya – BarcelonaTech, Barcelona, Spain
[b] International Center for Numerical Methods in Engineering (CIMNE), Barcelona, Spain

A B S T R A C T

The paper presents total-stress numerical analyses of large-displacement soil-structure interaction problems in geomechanics using the Particle Finite Element Method (PFEM). This method is characterized by frequent remeshing and the use of low order finite elements to evaluate the solution. Several important features of the method are: (i) a mixed formulation (displacement-mean pressure) stabilized numerically to alleviate the volumetric locking effects that are characteristic of low order elements when the medium is incompressible, (ii) a penalty method to prescribe the contact constraints between a rigid body and a deformable media combined with an implicit scheme to solve the tangential contact constraint, (iii) an explicit algorithm with adaptive substepping and correction of the yield surface drift to integrate the finite-strain multiplicative elasto-plastic constitutive relationship, and (iv) the mapping schemes to transfer information between successive discretizations. The performance of the method is demonstrated by several numerical examples, of increasing complexity, ranging from the insertion of a rigid strip footing to a rough cone penetration test. It is shown that the proposed method requires fewer computational resources than other numerical approaches addressing the same type of problems.

Keywords:
Penetration test
Large strains
Particle Finite Element Method (PFEM)
Cone penetration test

1. Introduction

Many activities in geotechnical engineering (probing, sampling, pile installation, ...) involve the insertion of a rigid body into the soil. In this kind of problem large displacements and deformations of the soil mass are always present. The coupled hydro-mechanical response of the soil adds further complexity, even in cases where insertion speed is tightly controlled. Analysis of problems of rigid body insertion into soil masses had traditionally relied on highly idealized approaches such as geometrically simple cavity expansion mechanisms [1]. Although much insight is gained from such analyses, a number of basic features of the problem are left aside and, as a consequence, a host of not fully understood empirical corrections and methods have been relied upon for practical applications.

Numerical simulation seems an obvious alternative to advance understanding in this area. However, the numerical simulation of rigid body insertion into soils is a complex task, since the system is full of non-linearities, contact-related, material-related and also geometrical. This latter kind of non-linearity was a fundamental obstacle to the Lagrangian or updated Lagrangian formulations of the finite element method (FEM) that are successful in other areas of geotechnical engineering. Strong mesh distortion resulted in large inaccuracies and/or stopped calculation at relatively small displacements [2].

In the last decades several numerical frameworks have been developed to address those problems. Some approaches are not based on continuum mechanics and use instead discrete element methods [3,4]; however, continuum-based approaches are dominant, particularly for fine-grained soils. Within continuum-based methods the approach most frequently applied to geotechnical insertion problems has been that of Arbitrary Lagrangian-Eulerian formulations (ALE). ALE finite element formulations combine the Lagrangian and Eulerian kinematic descriptions, by separately considering material and computational mesh motions [5].

The application of ALE to insertion problems in soil mechanics may be traced to Van den Berg et al. [6]. Afterwards, three main FEM ALE methods have been increasingly developed and repeatedly applied in this area: the so-called remeshing and interpolation technique by small strain (RITSS) developed by Randolph and co-workers [7–9], the so-called efficient ALE approach (EALE) developed by Nazem and co-workers [10–12] and the successive built-in implementation of ALE in Abaqus/Explicit, currently known as the Coupled Eulerian-Lagrangian (CEL) method [13]

* Corresponding author.
E-mail address: lluis.monforte@estudiant.upc.edu (L. Monforte).

which have been applied to insertion problems by several teams (e.g. [14–16]). A comparative review of these ALE methods has been recently presented by Wang et al. [17].

A second continuum-based numerical framework is that of the Material Point Method (MPM). A set of particles (material points) move within a fixed finite element computational grid. Material points carry all the information (density, velocity, stress, strain, external loads) which, at each step, is transferred to the grid to solve the mechanical problem. The computed solution allows updating of position and properties of the material points. The application of MPM to geotechnical problems is relatively recent [18,19]. Despite that, several implementations of MPM have been already used to model rigid body insertion into soils [20–22].

The Particle Finite Element Method (PFEM) is a third continuum-based approach that seems suitable to address geotechnical insertion problems. PFEM is actually an updated Lagrangian approach, but one that avoids mesh distortion problems by frequent remeshing. The nodes discretizing the analysis domain are treated as material particles the motion of which is tracked during the numerical solution. Remeshing in PFEM is based in Delaunay tessellations and uses low-order elements. PFEM was first developed to solve fluid-structure interaction problems [23] and then extended to other areas, like erosion, solid-solid interaction and thermo-plastic problems [24,25].

Carbonell et al. [26,27] first applied PFEM to geomechanical problems, extending the method to deal with tool-rock interaction problems in small and large scale excavations. In their work, however, material removal at the interface, rather than tool insertion was the focus. The excavated material was treated as a single-phase solid using a damage law as a constitutive model. Later, Salazar et al. [28], extended the code to include Bingham-like rheology to model flowslides.

Zhang et al. [29] presented a new PFEM implementation for granular flow applications, using a variational theorem to discretize the governing equations. A single-phase rigid plastic constitutive description of the soil was employed. An example of pipeline insertion into a Tresca soil was presented in Zhang et al. [29], however most applications have focused on soil flow problems [30,31].

This work documents an ongoing effort to develop a PFEM-based code for the analysis of solid insertion problems in soils. Monforte et al. [32] briefly illustrated how the code, named G-PFEM, is currently capable of handling coupled hydro-mechanical quasi-static problems in 2D using classic elasto-plastic soil constitutive descriptions (e.g. Cam clay). This paper focuses in a narrower range of applications: that of undrained problems, which may be analyzed using a total stress approach. G-PFEM has been implemented into Kratos [33] an object-oriented multi-disciplinary FE framework.

In the first part of this work a general description of the numerical method is given, with particular emphasis on the treatment of the contact between solid and soil and on the mapping procedures between successive meshes. In the second part of this work, the performance of the proposed approach is assessed solving three classical problems, of increasing complexity, for which previous solutions (numerical and/or analytical) were available: punching of a rigid strip footing from the surface, embedded T-bar motion and cone penetration test (CPT).

For reasons of space, not all algorithmic aspects of the method could be described here, and the reader is referred elsewhere to more in-depth treatment of some aspects. For instance, Monforte et al. [34] discuss in detail the performance of alternative mixed and stabilized formulations for G-PFEM, which are used to avoid the numerical problems induced by incompressibility (volumetric locking). The numerical schemes adopted for the integration of the constitutive equations have also been presented in more detail elsewhere [35].

2. Numerical method

This section addresses the numerical algorithms used in this work. After a brief review of the fundamentals of the Particle Finite Element Method, the large deformation displacement-mean pressure formulation for the problem is presented. The implementation of the constitutive equations and contact constraints are then briefly described. Finally, the interpolation procedures between different finite element meshes are explained.

2.1. Particle Finite Element Method (PFEM)

PFEM is a mesh-based continuum method: the solution is computed in a finite element mesh built with well-shaped low order elements. This computational mesh evolves during problem solution by means of frequent remeshing. A cornerstone of the PFEM implementation used here is an efficient remeshing strategy [23]. Basic tasks used in that strategy include adaptive inclusion of new nodes, Delaunay tessellation based on nodes and element smoothing. A Lagrangian description of the continuum is used and information between meshes is transferred using interpolation algorithms, later detailed. This general PFEM scheme is enriched with the inclusion of rigid bodies of specified motion that may contact, penetrate and reshape the discretized continuum.

In summary the solution algorithm involves the following steps:

1. Initialization. Discretize the domain with a Finite Element mesh. Define the shape and movement of the rigid structure.
2. Identify the external boundary. Search the nodes that are in contact or close to rigid bodies and initialize their contact conditions.
3. Compute some increments of the mechanical problem.
4. Construct a new mesh. This includes the introduction of new elements in areas with large plastic deformation, re-tessellation and some post-tessellation mesh smoothing.
5. State variables are interpolated from the previous mesh to the new one.
6. Go back to step 2 and repeat until problem-dependent stop condition.

The algorithm presented has some similitudes with other methods based on different approaches such as EALE and RITSS. A fundamental difference with EALE lies on mesh treatment. In EALE the number of nodes, elements and the topology of the FE mesh are preserved during the analysis and the boundary and interior nodes are relocated between solution steps by computing complementary elastic problems [10]. In contrast, the original idea of PFEM was to minimize nodal position changes during computation while constantly updating mesh topology using a Delaunay's Tessellation. Subsequently, in order to reduce the dependence of the solution on the initial discretization, additional adaptive techniques have been introduced: (i) insertion and removal of nodes based on plastic dissipation and (ii) improvement of mesh quality through Laplacian smoothing [25]. Despite these new features, modification of original nodal positions in PFEM remains relatively infrequent.

The remeshing aspect of PFEM makes it closer to RITSS, particularly in its first implementations [7,36]. In RITSS, periodical remeshing was performed using retriangulation, h-adaptive techniques and mesh smoothing. The algorithmic details are, however, different, particularly concerning retriangulation. The degree of adaptivity of some newer versions of RITSS that rely on Abaqus for mesh generation is perhaps more limited, as the role of users' experience was emphasized by Wang et al. [17]. The algorithms employed for transfer of information between successive meshes

in PFEM (see Section 2.6 below) are also different from those employed in RITSS.

Another significant difference is that whereas both RITSS and EALE use high-order elements to solve the governing equations (quadratic elements in RITSS and quadratic and higher in EALE); in the PFEM code presented here only linear elements are used. This, however, is not the only possible choice: Zhang et al. [31] used mixed elements with higher order interpolants. Other differences between the code presented here and previous approaches may also be a matter of choice, for instance the constitutive formulation using a multiplicative decomposition of the deformation gradient that is later presented (Section 2.3) has not been generally employed in RITSS or EALE, although, in principle, there is no major obstacle for it.

2.2. Governing equations

The current implementation of G-PFEM (i.e. Geotechnical-PFEM) contemplates only quasi-static problems. For the single-phase case presented here the linear momentum balance equation written in the current deformed configuration may be expressed as:

$$\begin{cases} \nabla \cdot \boldsymbol{\sigma} + \mathbf{b} = \mathbf{0} \\ \mathscr{M}(\mathbf{u}) = 0 \end{cases} \tag{1}$$

where $\boldsymbol{\sigma}$ is the Cauchy stress tensor, $\mathbf{b}$ are the external volumetric loads, $\mathbf{u}$ represents solid displacements and $\mathscr{M}$ stands for the initial conditions and the boundary conditions, that include fixed displacements and prescribed tractions.

The same problem may be restated with a mixed displacement - mean-pressure formulation (see [37]). Splitting the Cauchy stress between the deviatoric and volumetric part the problem reads:

$$\begin{cases} \nabla \cdot \boldsymbol{\sigma}^d + \nabla p + \mathbf{b} = \mathbf{0} \\ p - \frac{1}{3}\mathrm{tr}(\boldsymbol{\sigma}) = 0 \\ \mathscr{M}(\mathbf{u}) = 0 \end{cases} \tag{2}$$

where $\boldsymbol{\sigma}^d$ is the deviatoric part of the Cauchy stress tensor and p the Cauchy mean pressure.

The low order finite elements used in PFEM employ the same shape functions for displacement and mean pressure. At the incompressible limit they do not satisfy the Babuska-Brezzy conditions [37] and, as a consequence, volumetric locking may occur. Volumetric locking is characterized by a numerically-induced stiffer response of the system.

This problem may be bypassed by several strategies but the one best adapted to the method is to use a stabilized form of the mean-pressure equation that appears on the mixed formulation. The algorithm selected for stabilization is the so-called Pressure Laplacian technique (FPL, [37]). The FPL technique is also performant in consolidation problems [38], which may facilitate the extension of the code to coupled problems. Another suitable stabilization method is the so-called Polynomial Pressure Projection (PPP), previously applied for Stokes flow problems [39,40]. The former method has the advantage of not requiring mesh-size dependent numerical parameters. A detailed presentation of the implementation and performance of different numerical stabilization algorithms is given in [34].

Using a mixed formulation increases computational cost, since an extra degree of freedom (in this case, the pressure) is added at each node. On the other hand, linear elements reduce the number of gauss points, with important time saving advantages in the local stress integration step.

The discrete equations of the problem are obtained from the weak form of the problem defined in Equation (2) introducing the Finite Element shape functions. An Updated Lagrangian approach is used. The resulting quasi-static equations are integrated implicitly in time.

2.3. Constitutive equations

In the literature, two frameworks have been proposed for the formulation of large deformation elasto-plasticity [41].

The first one is based on an additive decomposition of the plastic and elastic strains and the use of hypoelastic rate constitutive models. This approach directly extends the usual small strains formulation and additional terms are added in order to deal with the rigid body rotation and ensure the objectivity of the resulting stress increment (e.g. Nazem et al. [10]). In the second approach, a multiplicative decomposition of the deformation gradient and hyperelastic response are assumed. This second approach is best suited to problems involving both large displacements and large deformations [42] and is the one adopted in G-PFEM.

The total deformation gradient, $\boldsymbol{F}$, is thus decomposed into an elastic and plastic part. The elastic part applies to an intermediate configuration of irreversible (plastic) deformation. Hence:

$$\boldsymbol{F} = \frac{\partial \boldsymbol{\varphi}(\boldsymbol{X}, t)}{\partial \boldsymbol{X}} = \boldsymbol{F}^e \cdot \boldsymbol{F}^p \tag{3}$$

The elastic deformation gradient may itself be decomposed into a volumetric and deviatoric part multiplicatively: $\boldsymbol{F}^e = \boldsymbol{F}^e_v \cdot \overline{\boldsymbol{F}}^e$; the volumetric part is given by $\boldsymbol{F}^e_v = J^{e\left(\frac{1}{3}\right)}\mathbb{1}$ and the deviatoric part by $\overline{\boldsymbol{F}}^e = \boldsymbol{F}^e \cdot (\boldsymbol{F}^e_v)^{-1}$ where $J^e = \det(\boldsymbol{F}^e)$ is the elastic Jacobian.

Elastic deformation is assumed hyper-elastic, with uncoupled volumetric and deviatoric responses,

$$\boldsymbol{\tau} = 2\boldsymbol{b}^e \frac{W(\boldsymbol{b}^e)}{\partial \boldsymbol{b}^e} = \boldsymbol{\tau}(\boldsymbol{b}^e) = Jp(J^e) + \boldsymbol{s}(\overline{\boldsymbol{b}}^e) \tag{4}$$

where $\boldsymbol{\tau}$ is the Kirchhoff stress tensor, related to the Cauchy stress through $\boldsymbol{\tau} = J\boldsymbol{\sigma}$ and $J = \det(\boldsymbol{F})$ is the determinant of the deformation gradient. W is the stored energy function, $\boldsymbol{b}^e$ the elastic left Cauchy Green tensor, $\boldsymbol{b}^e = \boldsymbol{F}^e \cdot \boldsymbol{F}^{eT}$, with its deviatoric part given by $\overline{\boldsymbol{b}}^e = \overline{\boldsymbol{F}}^e \cdot \overline{\boldsymbol{F}}^{eT}$.

In general the plastic part will require the specification of a yield criterion, f, a hardening law, h and a flow rule, g, in addition to the Kuhn-Tucker conditions [43]:

$$\begin{cases} f(\boldsymbol{\tau}, q) \leqslant 0 \\ q = h(\boldsymbol{F}^p \cdot \boldsymbol{F}^{pT}) \\ \boldsymbol{l}^p = \dot{\gamma} \frac{\partial g(\boldsymbol{\tau}, q)}{\partial \boldsymbol{\tau}} \end{cases} \tag{5}$$

where $f(\boldsymbol{\tau}, q)$ is the yield surface, q represents the hardening parameters, g is the plastic potential and $\dot{\gamma}$ stands for the plastic multiplier. Note that $\boldsymbol{l}^p = \boldsymbol{F}^e \cdot \overline{\boldsymbol{L}} \cdot (\boldsymbol{F}^e)^{-1}$ is the plastic velocity gradient defined in the final configuration whereas $\overline{\boldsymbol{L}} = \dot{\boldsymbol{F}}^p \cdot (\boldsymbol{F}^p)^{-1}$ is the plastic velocity gradient defined in the intermediate (plastic) configuration.

For the elastic-perfectly plastic analyses performed here, the hyperelastic model is given by

$$\begin{cases} p = \frac{2G(1+\nu)}{3(1-2\nu)} \frac{\ln J^e}{J} \\ \boldsymbol{s} = 2G \frac{\ln \overline{\boldsymbol{b}}^e}{2} \end{cases} \tag{6}$$

where G and ν are, respectively, the shear and Poisson modulus.

Plastic deformation is isochoric and, therefore, elastic and total volumetric strains coincide: $J = J^e J^p = J^e$ and $J^p = 1$. A perfectly plastic model with smoothed Tresca yield surface is employed [44]:

$$\begin{cases} f(\boldsymbol{\tau}, q) = J_2 \cos(\theta) - S_u \leqslant 0 \\ q = 0 \\ g = f \end{cases} \tag{7}$$

where J_2 and θ are the second invariant and the Lodes Angle of the Kirchhoff stress and S_u is the undrained shear strength.

2.4. Local integration

The robustness and accuracy of mechanical finite element analysis relies on the local integration scheme of the constitutive equations. When the multiplicative strain decomposition formulation is employed, the integration algorithm is usually implicit in time, leading to the return mapping algorithms [43,45]. Although implicit methods render second order convergence of the global problem [46], strong non-linear features of complex plastic models, such as high curvature of the yield surface, may lead to a lack of convergence of the local problem for a range of initial trial states [47].

In this work, an explicit integration scheme for multiplicative finite-strains elasto-plasticity is presented. This is based on the assumption of an exponential approximation of the variation of the plastic deformation gradient [43], from which the following explicit approximation is obtained:

$$\boldsymbol{F}^p_{n+1} = \exp(\Delta t\, \bar{\boldsymbol{L}}^p_n) \cdot \boldsymbol{F}^p_n \tag{8}$$

Then, introducing this equation to the definition of the total deformation gradient, Eq. (3):

$$\begin{aligned}\boldsymbol{F}_{n+1} &= \boldsymbol{F}^e_{n+1} \cdot \exp(\Delta t\, (\boldsymbol{F}^e_n)^{-1} \cdot \boldsymbol{l}^p_n \cdot \boldsymbol{F}^e_n) \cdot \boldsymbol{F}^p_n \\ &= \boldsymbol{F}^e_{n+1} \cdot (\boldsymbol{F}^e_n)^{-1} \cdot \exp\left(\Delta\gamma \frac{\partial g(\boldsymbol{\tau}, q)}{\partial \boldsymbol{\tau}}\right) \cdot \boldsymbol{F}_n\end{aligned} \tag{9}$$

Finally, the elastic Left Cauchy Green tensor is expressed as:

$$\begin{aligned}\boldsymbol{b}^e_{n+1} = \boldsymbol{F}_{n+1} \cdot \boldsymbol{F}_n^{-1} \cdot \exp\left(-\Delta\gamma \frac{\partial g(\boldsymbol{\tau}, q)}{\partial \boldsymbol{\tau}}\right) \cdot \boldsymbol{b}^e_n \\ \cdot \exp\left(-\Delta\gamma \frac{\partial g(\boldsymbol{\tau}, q)}{\partial \boldsymbol{\tau}}\right) \cdot \boldsymbol{F}_n^{-T} \boldsymbol{F}^T_{n+1}\end{aligned} \tag{10}$$

Note that this last equation defines the new elastic configuration (and stress state) in terms of quantities in the previous configuration, the new deformation gradient, obtained in the global scheme, and the plastic multiplier. The value of the plastic multiplier is obtained from the consistency condition.

In implicit methods a similar expression is obtained. In that case, the Hencky strain measure $\left(\boldsymbol{\epsilon}^e = \frac{\ln \boldsymbol{b}^e}{2}\right)$ is usually introduced and the obtained equations have the same formal structure of the small strains schemes. This is not the case of explicit methods: in the right hand side, the deformation gradient at time t_{n+1} and t_n have different eigenvectors and, thus, these terms do not commute. As a consequence, the logarithm of the right hand side is not equal to the sum of the logarithm of each term.

Explicit stress integration schemes render first order accuracy in time and, in elasto-plastic regime, the obtained stress state typically does not lay in the yield surface. To overcome these drawbacks, the integration of stresses at each Gauss point is governed with a numerical scheme based on Sloan et al. [48] that includes adaptive substepping and correction of the yield surface drift. More details on the implementation of this scheme can be found in [35].

2.5. Contact discretization

The interaction between multiple bodies produces a set of normal and tangential forces at the interface. Mathematically, contact conditions are expressed as a set of geometrical restrictions to the solution and the interaction forces are deduced from these constraints. In this work, one of the contacting bodies -the structure- is assumed to be rigid; this hypothesis is approximate enough when the Youngs moduli ratio between the structure and soil is large [49].

The geometrical constraints in the normal direction are that (i) penetration of the two bodies is not permitted, (ii) null normal force when the bodies are not in contact and (iii) only compressive normal force is allowed. These restrictions read:

$$\begin{cases} g_n \leqslant 0 \\ p_n > 0 \quad \text{if } g_n = 0 \\ p_n = 0 \quad \text{if } g_n < 0 \end{cases} \tag{11}$$

where g_n is the normal gap and p_n is the normal contact stress.

These constraints may be introduced into the solution of the problem by several methods. In this work, the penalty method is used; this way, a term proportional to the error on the constraint is added to the residual of the problem and the restrictions are only approximately fulfilled. In this case the normal contact force, $\boldsymbol{F}_n$, is expressed as:

$$\boldsymbol{F}_n = \begin{cases} \epsilon_n g_n w \boldsymbol{n} & \text{if } g_n \geqslant 0 \\ \boldsymbol{0} & \text{if } g_n < 0 \end{cases} \tag{12}$$

where ϵ_n is the normal penalty factor, w is the integration weight and $\boldsymbol{n}$ is the normal to the surface. As a consequence, a nodal contact force proportional to normal penetration is introduced at nodes of the contact surface of the deformable body.

The tangential part of the contact condition is elasto-plastic [50,51], where the so-called stick condition -no permanent tangential displacement between the two contacting bodies- corresponds to the elastic part and the slip condition - characterized by permanent relative tangential movement- is represented by the plastic flow. The elasto-plastic analogy is expressed as:

$$\begin{cases} \boldsymbol{g}_t = \boldsymbol{g}^e_t + \boldsymbol{g}^s_t \\ \boldsymbol{t} = \epsilon_t \boldsymbol{g}^e_t \\ f_s(\boldsymbol{t}, p_n, g_v) = |\boldsymbol{t}| - \bar{f}_s(p_n, g_v) \leqslant 0 \\ \dot{\boldsymbol{g}}^s_t = \dot{\gamma} \frac{\partial f_s}{\partial \boldsymbol{t}} = \dot{\gamma} \boldsymbol{n}_t \\ \dot{g_v} = \dot{\gamma} \end{cases} \tag{13}$$

where $\boldsymbol{g}^e_t$ and $\boldsymbol{g}^s_t$ are respectively the elastic and plastic parts of the tangential gap $\boldsymbol{g}_t$; $\boldsymbol{t}$ is the tangential contact stress, $\boldsymbol{n}_t = \boldsymbol{t}/||\boldsymbol{t}||$ and ϵ_t the tangential contact stiffness or penalty factor, f_s is the slip yield condition $\dot{\gamma}$ is the plastic multiplier and g_v is a hardening (strain-like) variable. In addition to these equations, the solution must fulfill the Kuhn-Tucker conditions.

The contact forces are calculated with an implicit integration procedure. The integration algorithm used to evaluate the tangential contact stress is detailed in Algorithm 1. It has the same formal structure than the well-known return mapping algorithm of elasto-plastic constitutive equations. First, a trial elastic step is computed as:

$$\begin{cases} \boldsymbol{t}^{trial}_{n+1} = \boldsymbol{t}_n + \epsilon_t \Delta \boldsymbol{g}_{n+1} \\ g^{trial}_{g,n} = g_{v,n} \end{cases} \tag{14}$$

where $\Delta \boldsymbol{g}_{n+1}$ is the increment of tangential gap in the time-step. The yield function is evaluated at this trial state; if it is lower or equal to zero the increment of displacement is purely elastic and no plastic slip appears.

Note that, for two-dimensional problems, all the vectors (tangential stresses and gaps) have the same direction, $\boldsymbol{n}_t$, so it is possible to simplify the expressions and use only the projection of the variables in this direction. Therefore the integration variable is scalar and not vectorial.

$$\begin{cases} (\boldsymbol{t}^{trial}_{n+1} \cdot \boldsymbol{n}_t) \cdot \boldsymbol{n}_t = t^{trial}_{n+1} \boldsymbol{n}_t = (t_n + \epsilon_t \Delta g_{n+1})\, \boldsymbol{n}_t \\ g^{trial}_{g,n} = g_{v,n} \end{cases} \tag{15}$$

Then, the problem reduces to finding the value of the plastic multiplier, $\Delta\gamma$, such that the stress state belongs to the plastic surface, $f_s(t_{n+1},\ p_n,\ g^v_{n+1}) = 0$, where:

$$\begin{cases} t_{n+1} = \epsilon_t g^e_{n+1} = \epsilon_t(g^e_n + \Delta g_{n+1} - \Delta g^s_{n+1}) = t^{trial}_{n+1} - \epsilon_t \Delta\gamma \\ g_{v,n+1} = g^{trial}_{v,n+1} + \Delta\gamma \end{cases} \tag{16}$$

The tangent matrix may be obtained as:

$$d\boldsymbol{t} = \frac{H\epsilon_t}{H+\epsilon_t}\boldsymbol{n}_t dg - \frac{\epsilon_t}{H+\epsilon_t}\frac{\partial f_s}{\partial p_n}\boldsymbol{n}_t dp_n \tag{17}$$

where $H = -\frac{\partial f_s}{\partial g_v}$ and $d\boldsymbol{p}_n = \epsilon_n\, dg_n$.

Algorithm 1. Implicit integration of the contact tangential stresses.

Data: $\Delta g_t,\ p_n,\ t_n$

Trial State:

$t^{trial}_{n+1} = t_n + \epsilon_t \Delta g_t$

$\Delta\gamma = 0$

$g^{trial}_{v,n+1} = g_{v,n}$

if $f_s(t^{trial}_{n+1}, p_n, g^{trial}_{v,n+1}) < 0$ **then**

  Elastic step:

  $t_{n+1} = t^{trial}_{n+1}$

  $g_{v,n+1} = g^{trial}_{v,n+1}$

else

  Plastic Step:

  $i = 0$

  $f^{(i)}_s = f_s(t^{trial}_{n+1}, p_n, g^{trial}_{v,n+1})$

  while $\|f^{(i)}_s\| > Tol_f$ **do**

    $\delta\gamma = \frac{f^i_s}{\epsilon_t - \frac{\partial f}{\partial g_v}}$

    $i = i + 1$

    $\Delta\gamma^{(i)} = \Delta\gamma^{(i-1)} + \delta\gamma$

    $t^{(i)}_{n+1} = t^{trial} - \epsilon_t \Delta\gamma^{(i)}$

    $g^{(i)}_{v,n+1} = g^{trial}_v + \Delta\gamma^{(i)}$

    $f^{(i)}_s = f_s(t^{(i)}_{n+1}, p_n, g^{(i)}_{v,n+1})$

  end

end

Result: $t_{n+1},\ g_{v,n+1}$

2.6. Mapping between evolving meshes

One of the main difficulties encountered in adaptive methods is the transfer of information between different discretizations. In G-PFEM information is transferred between the previous mesh and the newly constructed one at every remeshing stage. Nodal variables (displacements and mean pressure) are mapped into the new mesh using the previous mesh shape functions.

Note that for the simple constitutive model employed here, the only internal variables that need mapping are the deviatoric part of the Elastic Left Cauchy Green tensor and the determinant of the deformation gradient (Jacobian). Through the hyperelastic model these two variables uniquely determine the Cauchy Stress tensor.

Two different transfer operators have been used. The algorithms selected share a common trait: when an element of the old mesh is preserved, the new value of the variable coincides with the value on the previous mesh. The first method consists simply on copying to each element of the new mesh the information of the element of the previous mesh whose centroid is nearest to the centroid of the new element. In the second strategy, a least square interpolation procedure is used [52]: let T_i and $\overline{T}_k$ be some internal variable in the new and previous mesh; a piecewice constat interpolation of these variables over the whole domain is constructed, $T = T_i w_i$ and $\overline{T} = \overline{T}_k \overline{w}_k$, where the interpolation functions w_i and $\overline{w}_k$ are equal to the unity in elements i and k of the new and old mesh and zero elsewhere.

The value of the internal variable in the new mesh is computed solving the following problem:

$$T_i = \arg\left(\min_{T_i}\left(\int_\Omega (T_i w_i - \overline{T}_k \overline{w}_k)^2 d\Omega\right)\right) \tag{18}$$

After carrying out the minimization, the following explicit expression is found for the new value of the internal variable for one integration point elements:

$$T_i = \frac{\overline{T}_k \int_\Omega \overline{w}_k w_i\, d\Omega}{\int_\Omega w_i\, d\Omega} \tag{19}$$

Therefore, the value of the internal variable on an element of the new mesh is the mean value of the variable of the elements of the previous mesh that overlaped that position, averaged by the area of overlapping. This algorithm is implemented using the super-mesh concept [53].

Only the first transfer algorithm ensures that the new state is admissible (using the second algorithm the stress state may be outside of the yield surface); none of the two guarantee that the deformable body is in equilibrium. The first problem is directly tackled applying a yield surface drift correction algorithm if the stress state lies outside the yield surface. Possible errors due to out-of-balance forces after remeshing are ignored and a time-step is advanced before mechanical equilibrium is again imposed. In this respect the method appears again as closer to RITSS than to EALE [10,54].

3. Application examples

In this section several examples of increasing numerical complexity are presented to illustrate the performance of the method. The first one involves the penetration of a perfectly rigid rough footing into a soil and it is used to discuss the influence of remeshing procedures. Afterwards, results of two important penetration problems involving contact interface slip of increasing difficulty, namely the T-Bar and the CPT, are reported to assess the accuracy and robustness of the numerical method.

3.1. Strip footing on clay

A first example involves the computation of bearing capacity for a strip footing lying on a weightless uniform Tresca soil (Fig. 1), pushed to a depth equal to the footing width. The contact algorithm is not yet involved, because instead of simulating the footing as a rigid body the problem is simplified prescribing a uniform vertical displacement as boundary condition. The example is used instead to illustrate the benefits of the stabilization procedure

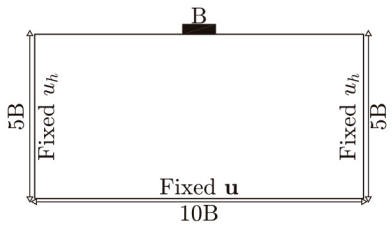

Fig. 1. Problem definition: a strip footing on undrained soil layer.

and to explore the influence of the different mesh mapping schemes described above. As this problem has been frequently addressed in the literature, it does also allow some comparisons with other numerical approaches.

As shown in Table 1, the first 5 cases analyzed differ in several numerical aspects: formulation of the governing equations, mapping rule, number of elements at the beginning and at the end of the simulation. The mixed stabilized formulation of the governing equations was applied in all cases, except in PFEM_F_1, where a displacement only formulation was used. The stabilized cases differed in the choice of initial mesh and in the mapping procedure applied between successive meshes.

The terminology used to label the different meshes employed was inspired by Kardani et al. [12]. For instance, the coarse discretization employed for cases PFEM_F_1 and PFEM_F_2 used twice the number of nodes of Kardani et al. coarse case (the difference arising because here the symmetry of the problem was not used to reduce the model).

All these cases used the same set of material parameters, also taken from Kardani et al. [12] and are characteristic of a very soft clay ($E = 100$ kPa, $S_u = 1$ kPa, $\nu = 0.495$). These values imply a rigidity index, I_r, of 33. The rigidity index is defined as the ratio between the shear modulus, $G = \frac{E}{2(1+\nu)}$, and the undrained shear strength, S_u.

Fig. 2(a) presents curves of normalized settlement vs normalized soil resistance for these 5 cases. The normalized limit resistance provides a bearing capacity factor for this problem, $N_c = \frac{q_u}{S_u}$, where q_u is the vertical stress applied by the footing and S_u the strength of the soil.

The first thing to note is that the curve obtained using the displacement only formulation (PFEM_F_1) is much higher than those obtained using the mixed stabilized formulation. This is a consequence of the spurious increase in stiffness that results from volumetric locking. Indeed, the oscillations on the mean-pressure field caused by this problem became so severe that the computation of this case could not be finished.

The other four cases show a very similar response. Normalized load-displacement curves show some small oscillations that are mostly due to the lack of equilibrium of the interpolated fields after remeshing. It is apparent that these oscillations remain controlled. Neither the coarseness of the initial mesh, (compare PFEM_F_2 and PFEM_F_3), nor the enforcement of problem symmetry, (compare PFEM_F_3 and PFEM_F_5), seem to have much influence in the solution.

The mapping algorithm came more into play for simulations using the initially coarser mesh (termed X-coarse or extra-coarse), because there mesh refinement was more pronounced (Fig. 3(d)). Again, the effect of this numerical choice on the solution was minimal. Because of the good performance of nearest-neighbor interpolation and its relatively smaller computational cost, this strategy was adopted in all the following examples.

It is interesting to compare these results with those of a parametric study of the same case presented by Kardani et al. [12] using the EALE method. They analyzed the problem with different higher-order elements (6-node, 15-node and 21 nodes) using structured meshes in which the number of degrees of freedom was maintained constant hence trading element order for number of elements. Two levels of discretization were explored, a coarse mesh with 3721 nodes and a fine one with 14,641 nodes. The

Table 1
Characteristics of the G-PFEM simulations for the strip footing example.

Case	Formulation	Mapping	Initial Mesh	Initial number of elements	Final number of elements	N_c ($z/B = 1$)
PFEM_F_1	Displacement (u-only)	Centroid	Coarse	14,427	14,556	9.34 (at $z/B = 0.25$)
PFEM_F_2	Mixed stabilized (u-p)	Centroid	Coarse	14,427	14,601	7.14
PFEM_F_3	Mixed stabilized (u-p)	Centroid	X-Coarse	1669	4669	7.04
PFEM_F_4	Mixed stabilized (u-p)	Least Square	X-Coarse	1669	4977	7.17
PFEM_F_5	Mixed stabilized (u-p)	Centroid	Half X-Coarse	832	2551	7.16

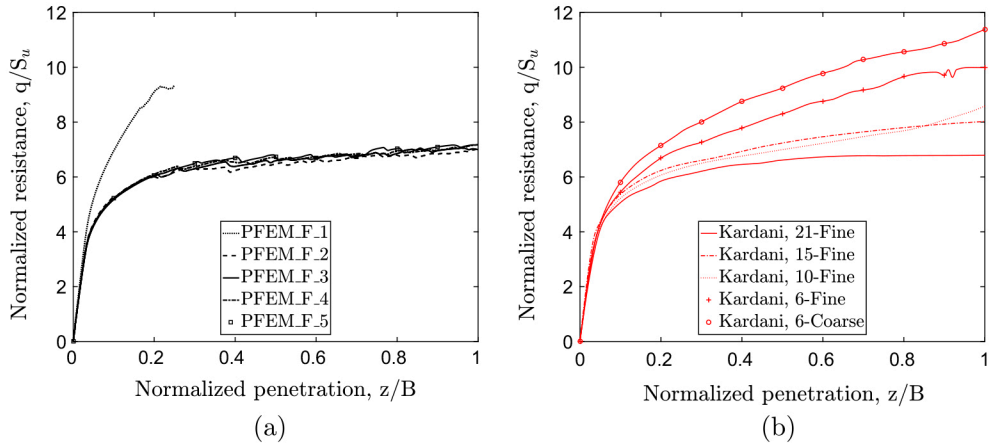

Fig. 2. Rigid footing penetration on Tresca soil. Effect of different numerical options on the normalized load settlement curves. $I_r = 33$ for all cases (a) G-PFEM parametric analyses (see Table 1) (b) EALE parametric analyses presented by Kardani et al. [12] (see Table 2 for details).

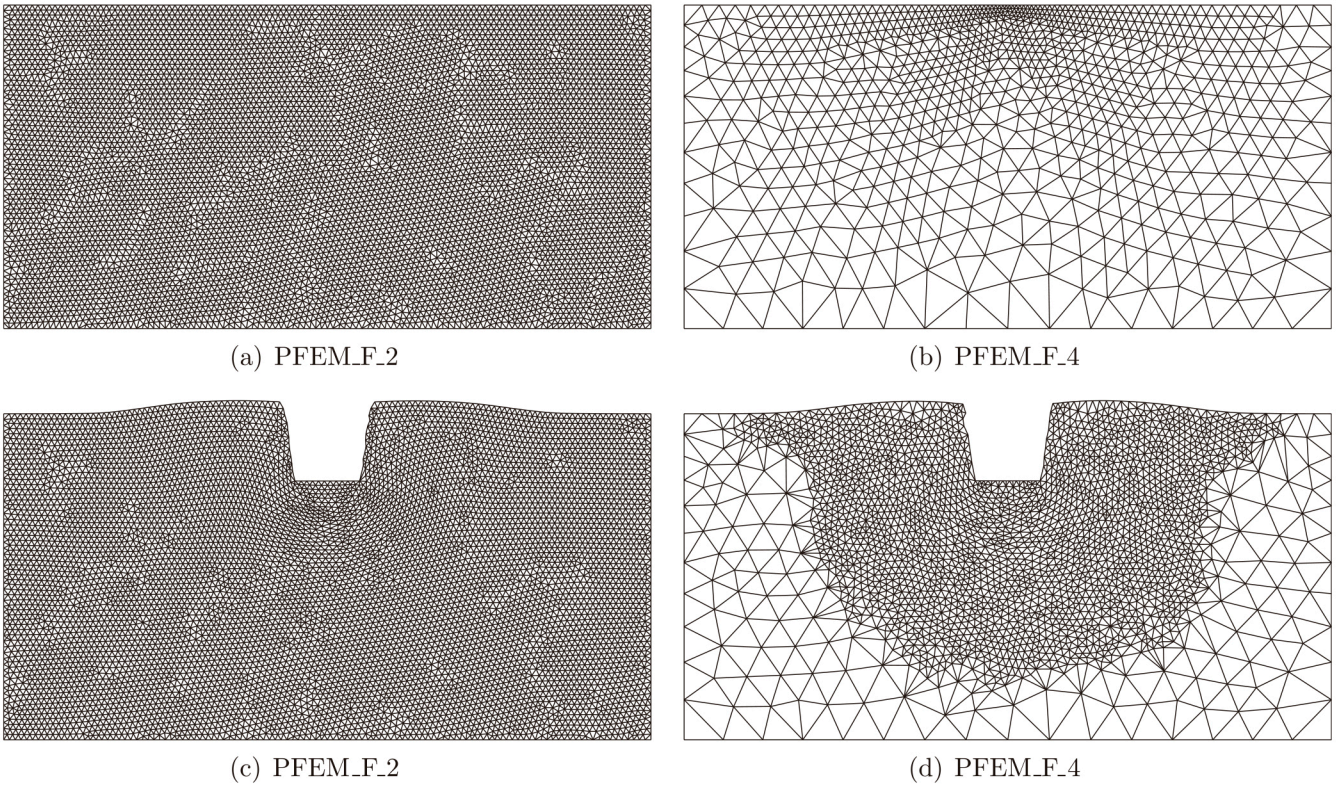

Fig. 3. Initial, (a) and (b), and final, (c) and (d) mesh for two different initial discretizations of the footing problem.

results obtained in several of their analyses are reproduced here as Fig. 2(b).

The stiffer response obtained in EALE with smaller-order elements may be interpreted as an effect of volumetric locking. It is well-known that one possible strategy to attenuate locking is, precisely, to increase the interpolation order of the elements. This, however, adds some extra computational cost. Table 2 presents a comparison of computational cost indicators (interpolation order, degrees of freedom, Gauss points) for this EALE models and model PFEM_F_5 -the one closer in geometry, as all the EALE models had imposed symmetry. It would seem that for this type of problem GPFEM offers some computational advantage: similar performance is obtained with order of magnitude savings on integration point numbers and d.o.f.

A separate parametric analysis of this case has been performed to explore the effect of the rigidity index on the solution. The base model used in the analysis is PFEM_F_3. The undrained shear strength and Poisson ratio is kept constant and Young modulus is varied to cover a range of I_r between 16 and 500, (16, 33.4 167 and 500).

Fig. 4(a) shows the normalized load vs penetration curves that result from this analysis. As may be expected, the effect of rigidity index is very pronounced at the beginning of the loading, becoming less important as penetration progresses. The analysis was stopped at a penetration depth equal to footing width (1 m). At that stage the normalized resistance is similar for all the cases, between 6.9 and 7.3; larger values are encountered as the rigidity index increases.

In soils with low rigidity index, the first loading steps are dominated by elastic loading. For example, in the case of a rigidity index of 16, the first plastic gauss point appears at a normalized penetration depth of $z/B = 0.05$ and the failure surface does not reach the ground surface at the end of the computation (Fig. 5 (a)). On the other hand, with a rigidity index of 500, the first plastic gauss point appears at a $z/B = 0.001$ (that is, at the first computational step), and the failure mechanism reaches the ground surface at $z/B = 0.014$; this point corresponds to the drastic change of slope of the penetration curve (Fig. 4(a)). The small effect of rigidity on the bearing capacity factor for the large strain analyses is more clearly illustrated in Fig. 6.

Fig. 4(b) shows the result of a similar parametric analysis conducted by Sołowski and Sloan [20] using a MPM method. The results obtained are remarkably similar (Fig. 6). Because the methods are quite different it is difficult to compare performance

Table 2
Indicators of computational cost and bearing capacity factor for solutions of the strip footing example. Data for the EALE models is taken from Kardani et al. [12].

Case	Elements	Interp. order	Degrees of freedom		Gauss points		N_c
			Initial	Final	Initial	Final	$(z/B = 1)$
PFEM_F_5	3-noded triangle	1	1371	3978	832	2551	7.16
EALE-6-Coarse	6-noded	2	7442	7442	10,800	10,800	11.38
EALE-6-Fine	6-noded	2	29,282	29,282	43,200	43,200	9.99
EALE-10-Fine	10-noded	3	29,282	29,282	19,200	19,200	8.59
EALE-15-Fine	15-noded	4	29,282	29,282	21,600	21,600	8.02
EALE-21-Fine	21-noded	5	29,282	29,282	18,432	18,432	6.73

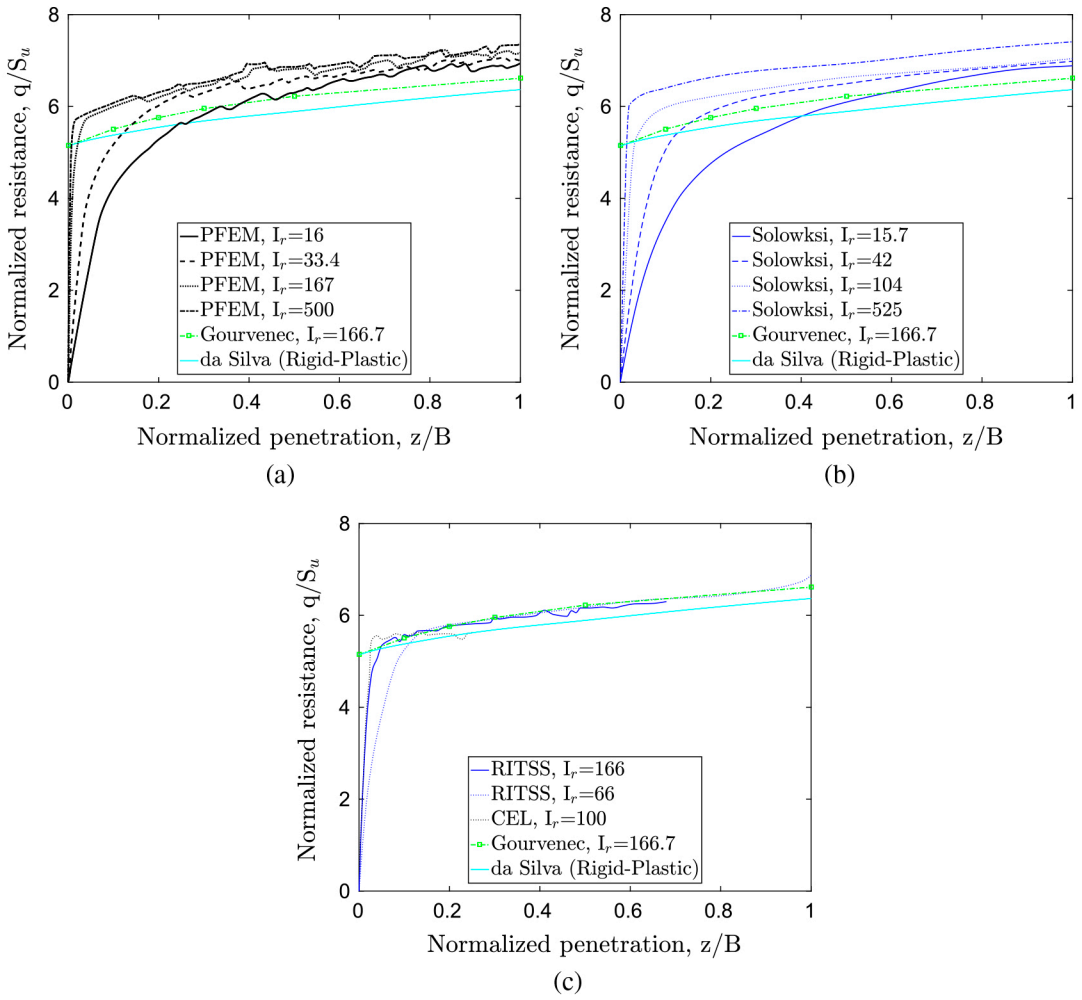

Fig. 4. Rigid footing penetration on Tresca soil. Effect of rigidity index on the normalized load settlement curves. (a) G-PFEM parametric analyses using model PFEM_F_3 (see Table 1) (b) MPM parametric analysis by Sołowski and Sloan [20] (c) ALE results.

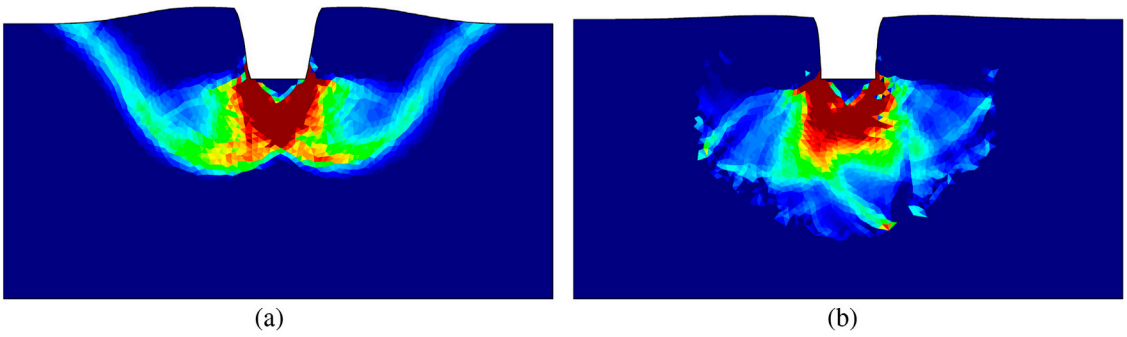

Fig. 5. Strip footing on undrained soil layer. Magnitude of the Plastic deviatoric incremental strain at $z/B = 1$ for case $I_r = 500$, (a), and $I_r = 16$, (b).

through indicators. Sołowski and Sloan [20] obtained those results using a model with 60,000 grid cells, requiring 46 h of machine time (3.4 GHz single core). The PFEM simulations presented in Fig. 4(a) required between 0.5 and 3.5 h of machine time (1.8 GHz × 4).

In Figs. 4 and 6 are also plotted the values obtained by Silva et al. [55] using sequential limit analysis, for a rigid-plastic material. Although they describe the formulation used as an upper bound the penetration curve lies below the large deformation ones once these enter the plastic regime. Interestingly, the small-strain wished-in-place analyses presented by Gourvenec and Mana [56] lie between the rigid-plastic and large strain results.

Finally, for completeness, Fig. 4(c) presents results for the same problem using other ALE-based methods (RITSS [57,58], CEL [59]). The RITSS computations show good coincidence with the results of the small-strain wished-in-place results of Gourvenec and Mana [56]. That coincidence is somewhat perplexing, since small strain analyses cannot represent the effect of the small, but noticeable, surface heave that accompanies footing penetration (Fig. 3). The CEL computation stops earlier and shows almost no increase after

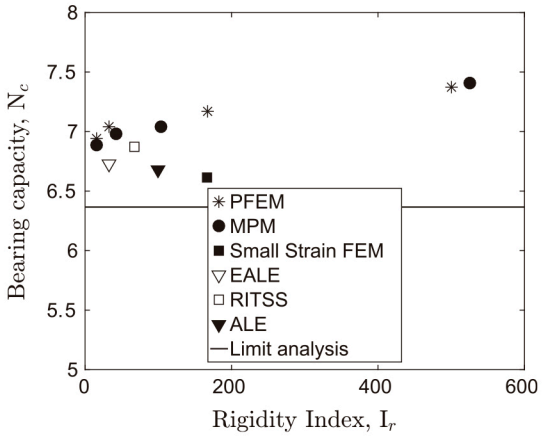

Fig. 6. Influence of analysis type on bearing capacity factor at $z/B = 1$.

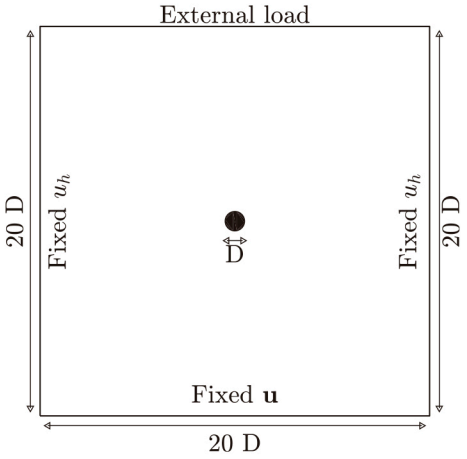

Fig. 7. Problem definition: a T-bar inserted in an undrained soil layer.

a penetration of $z/B \approx 0.03$; this behavior may be due to the relatively small soil domain considered (only $B \times 2B$, assuming symmetry), far smaller than the extension of the active plastic zone encountered using PFEM (Fig. 5).

3.2. T-bar

In this example, the displacement of an embedded T-bar is studied assuming plane strain. The penetrometer is placed in the middle of a square domain of 20 times the T-bar diameter (Fig. 7). The horizontal displacement is restricted in the vertical boundaries and the bottom boundary is fixed. At the beginning of the simulation, the soil is undisturbed; a vertical stress of 100 kPa is applied to the upper boundary to ensure the contact

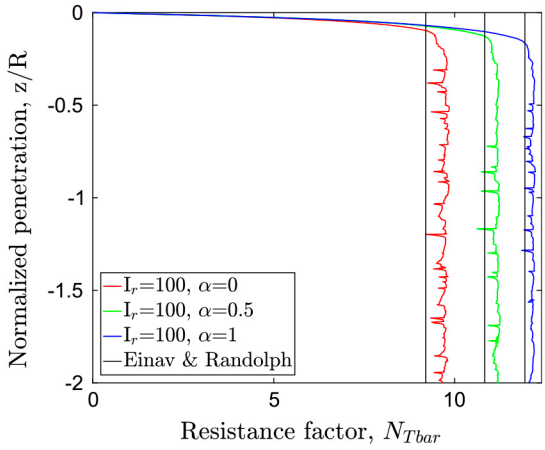

Fig. 8. Effect of contact roughness on normalized penetration curves for the T-Bar. Thin black lines: upper bound-strain path solution of Einav and Randolph [60].

between the whole penetrometer and the soil throughout the simulation. K_0 is 0.95. The soil is weightless and characterized by undrained strength $S_u = 10$ kPa, a Poisson's coefficient equal to 0.49 and a shear modulus of 1000 kPa (hence $I_r = 100$).

Interface tangential slip follows a von Mises yield criterion (i.e. $f_s = t - \alpha S_u$). The maximum shear strength admissible between the soil and rigid body interface is a fraction α of the undrained shear strength of the soil. A parametric analysis is then performed on the effect of interface roughness.

In this problem the contact nodal density (i.e. the number of nodes in contact with the rigid structure) plays a significant role in the accuracy of the solution. A characteristic length, h, is defined so that a new node is inserted midway between two contacting nodes if the distance between them is larger than h. Coarsening i.e. contact node removal takes place when the distance between two adjacent contact nodes is smaller than $\beta h/2$, where $\beta < 1$ is the coarsening parameter.

Fig. 8 shows the normalized penetration vs resistance curves for the simulations of the embedded T-bar. For this analysis, the main result of interest is the resistance factor, N_{Tbar}, defined as the total vertical force acting on the T-bar divided by the projected area, plotted against normalized penetration. The curves are punctuated by periodic drops. These correspond to interface remeshing events. As indicated in Table 3 the variability induced by this numerical noise on the capacity estimate is small, with coefficient of variation (Standard Deviation/Mean) below 1%. For all of these analyses the characteristic length value was fixed at $h = 0.28R$, where R is the T-bar radius; as a result the number of nodes in contact with the bar varied between 22 and 55 nodes. The initial overall node number is the same for all cases (1175) and does not change very much during simulation.

The dependence of N_{Tbar} on interface roughness that is obtained from these simulations is plotted in Fig. 9, where it is compared

Table 3
T-bar PFEM simulations. Discretization details and T-bar factor (mean and standard deviation, STD). Initial number of nodes 1175, initial number of elements 2199.

Refinement	Roughness factor, α	N_{Tbar}			Characteristic length, h	Interface nodes (Nmin-Nmax)	Final number of nodes	Final number of elements
		Mean	STD	UB [60]				
Reference	0	9.71	0.083	9.20	0.28	22–55	1040	1923
Reference	0.25	10.48	0.065	10.09	Idem	22–55	1191	2221
Reference	0.5	11.16	0.617	10.83	Idem	22–55	1302	2501
Reference	0.75	11.71	0.062	11.46	Idem	22–55	1080	2656
Reference	1	12.14	0.048	11.94	Idem	22–55	1259	2418
Intense	0	9.45	0.029	9.20	0.12	50–125	2215	4087
Reduced	0	9.77	0.105	9.20	0.34	18–46	704	1257

with previous upper bound results [60] as well as with small strain (Updated Lagrangian) FE solutions [61] and RITSS results [62]. The results obtained with G-PFEM are slightly above (between 1.2% and 5.5%) the plasticity upper bound solution, with a smaller discrepancy for larger interface roughness values.

These observed discrepancies are mostly a byproduct of the relatively coarse mesh employed in the simulations. A numerical exercise was performed to prove this: two more cases were run at 0 interface roughness in which the only change was in the interface characteristic length, h. In one case $h = 0.12R$ and contact refinement was more intense than in the reference case, whereas in other $h = 0.34R$ and contact refinement was reduced.

The results of this exercise are presented in Fig. 10(b). A more intense discretization of the interface contact has direct impact on the N_{Tbar} factor, which becomes closer to the UB limit as the refinement proceeds (Fig. 10(a)). The trend of the G-PFEM simulations, in this respect, is aligned with a previous RITSS result [62]. It does also have a direct impact on the smoothness of the numerical solution (Fig. 10(b)), which increases with contact refinement. Finally (Fig. 11) it does also allow more precise definition of the full flow mechanism [61].

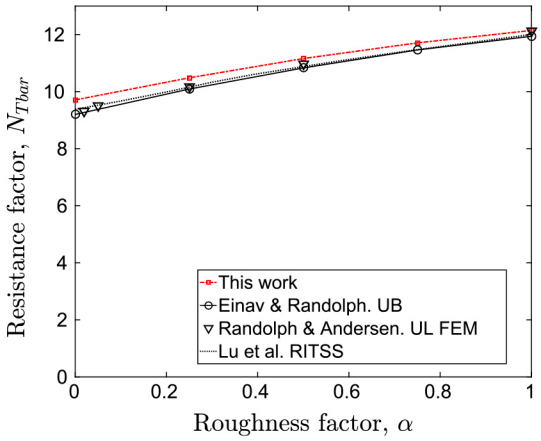

Fig. 9. Dependence of N_{Tbar} factor on surface roughness for the G-PFEM simulations and previous.

3.3. CPT

In this section, the proposed numerical technique is applied to an axisymmetric case: the cone penetration test (Fig. 12). A CPT with standard dimensions (D = 35.7 mm; apex angle 60°) is pushed 25 radii into a weightless Tresca material. In order to bypass the numerical problems that arise at the first steps of the calculation, when only a node of the soil is in contact with the rigid structure, the cone tip starts from a prebored situation, at a depth of 2.8 radii.

No initial stress is imposed in the soil domain, hence the initial stress state is isotropic. Identical constitutive parameters to those in the previous example are used ($S_u = 10$ kPa; $\nu = 0.49$; $I_r = 100$). These conditions also allow comparisons with previously reported work on the same problem. Both the cone tip and the whole shaft are rough. A parametric study is carried out on the effect of interface roughness.

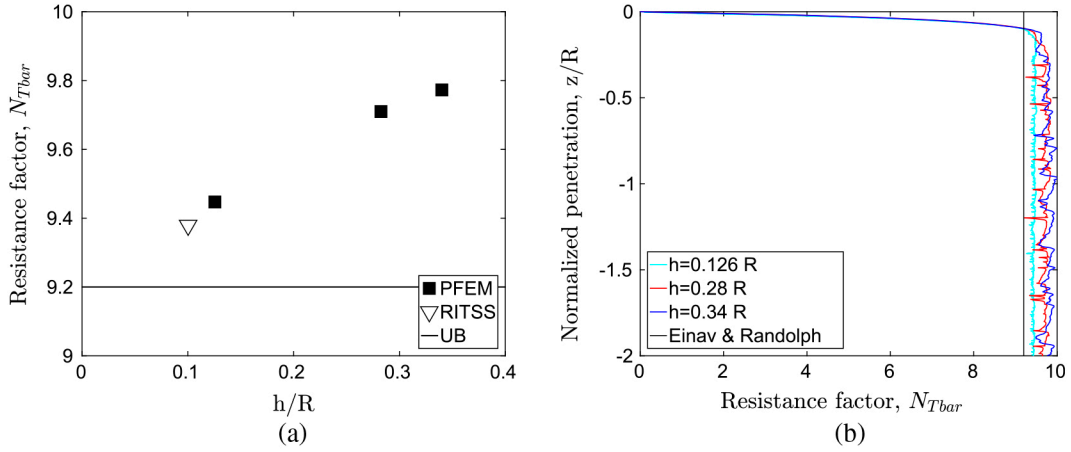

Fig. 10. Effect of characteristic nodal refinement length (h) on the embedded T-bar simulation (a) on the N_{Tbar} factor (b) on the penetration curve.

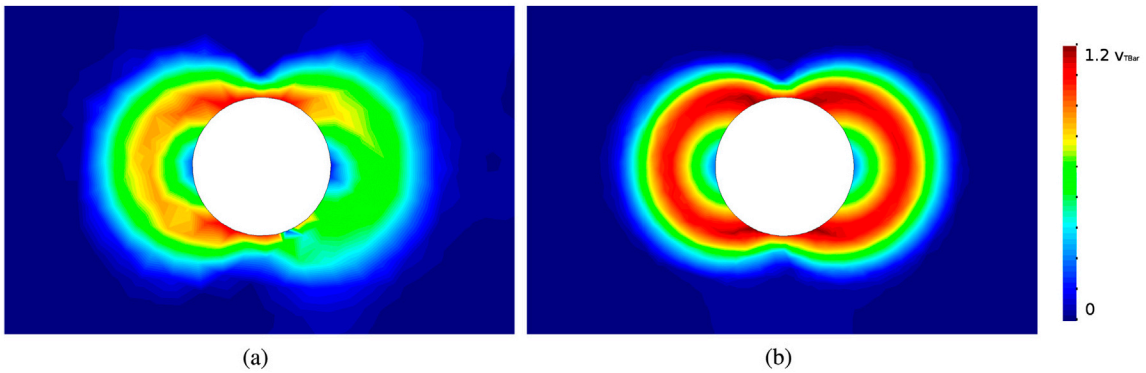

Fig. 11. T-bar. Contour plot of the magnitude of the velocity for the smooth contact case for (a) the reference refinement parameter $h = 0.28R$ (b) the intense refinement setting $h = 0.12R$.

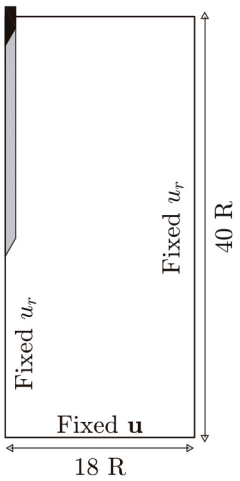

Fig. 12. Problem definition: Cone Penetration Test. Outlined in black is the initial position and in gray the final one.

The relevant bearing capacity factor in this case is given by the cone factor $N_{kt} = \frac{q_c - \sigma_v}{S_u}$. Cone tip resistance, q_c is computed adding vertical forces from nodes at the cone tip. Vertical forces are also integrated on a shaft length 7.5 radius behind the cone tip to evaluate sleeve friction.

Fig. 13 shows the evolution of cone factor and sleeve friction vs normalized depth for different adhesions (ranging from 0 to 0.7 S_u). All the cone factor curves seem to reach a steady state at around 20 penetration radii. It is worth noting that all the differences appear within the first penetration radius; afterwards all the curves seem parallel. As expected, the resistance in the friction sleeve is equal to the imposed adhesion.

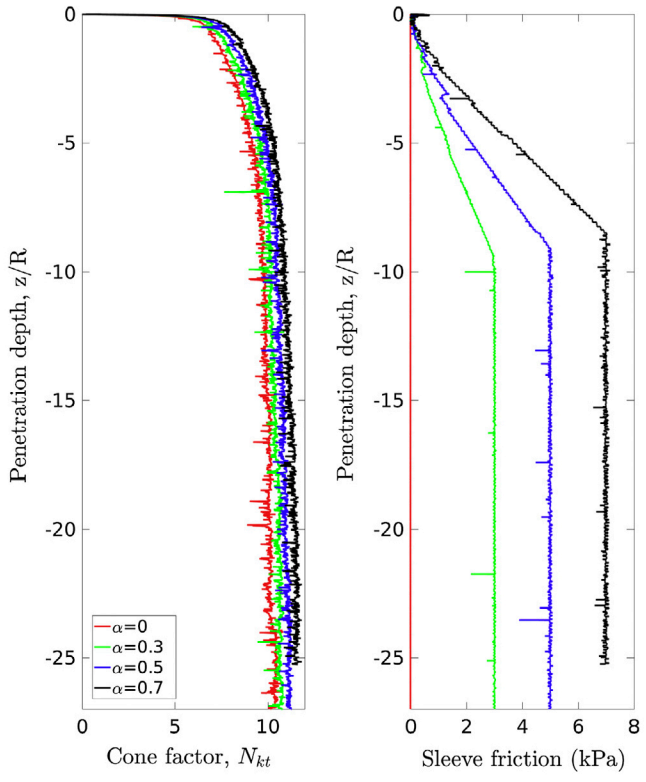

Fig. 13. Effect of contact roughness on CPT response for a rigidity index of 100 on unstressed Tresca soil. Left hand side normalized tip resistance (cone factor). Right hand side: sleeve friction.

There has been much previous work on this problem [63,64,8,65]; which has been also used for benchmarking purposes [17]. In general, tip resistance depends on cone roughness, on initial stress anisotropy and on the rigidity factor. For the isotropically stressed, smooth, $I_r = 100$, case Table 4 compiles previously reported cone factors, which show some variation. Some of the differences reported can be attributed to the different yield envelope used: many computations employ a Mises envelope, a shape less realistic for soils but more computationally-friendly than the Tresca model. When using the same method, computations using a Mises strength envelope result on smaller cone factors by about 10% (something similar had been observed for the T-bar problem by Lu et al. [62]). The value obtained using G-PFEM is well within the range obtained in other computations using a Tresca model.

As roughness increases, the cone factor at steady state increases almost linearly. The gradient of the variation of the cone factor as the roughness increases is 1.8; this value is within the range of previous analyses (see Fig. 14). A detailed analysis of the numerical reasons for the observed variation in this slope is beyond the scope of this work.

The initial mesh employed in the CPT analysis is illustrated in Fig. 15. The characteristic length, h was again $0.28R$, R now being the radius of the cone. Because the contact surface was longer, the model was more demanding in terms of mesh refinement that of the T-bar and by the end of the computation the number of

Table 4
Comparative cone factors for a smooth cone ($\alpha = 0$) penetrating a $I_r = 100$ soil under isotropic confinement.

Reference	Method	N_{kt}	Failure criteria
Teh and Houlsby [63]	Strain path method + FE	9.4	Mises
Walker and Yu [14]	CEL	9.5	Mises
Wang et al. [17]	CEL	11.1	Mises
Wang et al. [17]	EALE	10.2	Mises
Wang et al. [17]	RITSS	9.8	Mises
Van den Berg [64]	ALE	11	Tresca
Lu et al. [8]	RITSS	10.77	Tresca
Beuth [65]	MPM	10.2	Tresca
This work	G-PFEM	10.26	Tresca

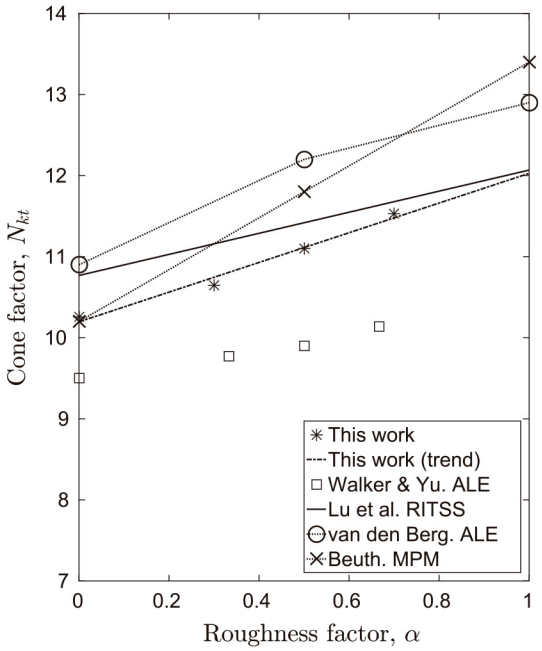

Fig. 14. Influence of contact roughness on cone factor N_{kt}.

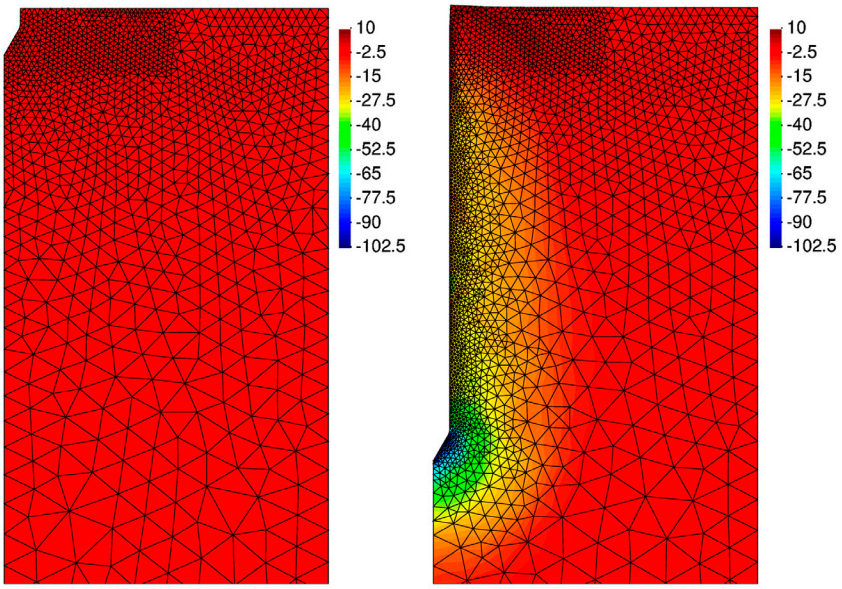

Fig. 15. Mean stress field (kPa) and mesh for the $\alpha = 0.0$ case at the initial and final stages of the computation.

Table 5
G-PFEM CPT simulations discretization details, Cone Factor (mean and Standard Deviation) and Friction Ratio (mean value and Standard deviation).

	Roughness factor	Initial number of nodes	Initial number of elements	Final number of nodes	Final number of elements	Cone factor		Friction ratio		Lu et al. RITSS [8]
						Mean	STD	Mean (%)	STD	
CPT0	0	1360	2485	2501	4650	10.26	0.1792			10.77
CPT3	0.3	1360	2485	2526	4696	10.64	0.1171	2.45	$4.19 \cdot 10^{-4}$	11.16
CTP5	0.5	1360	2485	2595	4823	11.11	0.1227	4.50	$6.69 \cdot 10^{-4}$	11.42
CPT7	0.7	1360	2485	2407	4476	11.53	0.1212	6.07	$0.18 \cdot 10^{-4}$	11.68

elements had roughly doubled (Fig. 15(b) and Table 5). The finer mesh used here results in a very small numerical oscillation, with coefficient of variations for the cone factor of around 1% and even smaller for sleeve friction.

Although the mesh used is relatively fine, the computational load remains moderate. The initial mesh is composed by 1360 nodes and 2485 elements whereas the coarser final mesh has 2595 nodes and 4823 elements (Table 5). For reference, Wang et al. [17] used 5000 quadratic elements in their EALE mesh, whereas Beuth [65] used more than 20,000 elements and one order of magnitude more material points, (a 20° slice of the axisymmetric problem was simulated in 3D).

4. Conclusions

This work has presented a numerical framework for the simulation of total stress analysis problems in geomechanics using the Particle Finite Element Method (PFEM). This method is based on an updated Lagrangian Finite Element method, using low-order elements and frequent remeshing. In order to bypass the drastic volumetric locking of low-order elements in the incompressible limit, a stabilized displacement-mean pressure formulation is employed. Contact constraints are discretized with a penalty method and the tangential part is modeled by an elasto-plastic model; contact tangential stresses are integrated implicitly and the developed algorithm retains the formal structure of one dimensional return mapping.

The method performance has been illustrated by means of several numerical examples. In the first one, the penetration of a rigid strip footing, it has been shown that stabilized formulations alleviate the severe volumetric locking that suffer low order elements; in addition, the effects of rigidity index on the penetration response appear to be well captured. In the T-bar and CPT examples the contact algorithm comes into play. The degree of interface refinement has an important effect on the precision of the numerical solution. Interface refinement is easy to control and adapt to the requirements of the specific problem being analyzed. Despite using relatively coarse meshes, the results obtained agree well with previous analyses using other methods.

It appears that the numerical strategy followed by G-PFEM, using adaptive low-order discretization of the domain, obtains similar results than those attained with alternative numerical methods with significant savings in computational effort. The current implementation is also capable of handling coupled analysis, and benchmarking of that capability is the object of current development. Furthermore, since G-PFEM has been built in the general-purpose FE Kratos environment, extension of its current capabilities to other scenarios (dynamic, fluid-soil interaction, thermal) would seem relatively straightforward.

Acknowledgments

This work has been supported by the Research Directorate of Spain (DGICYT) through research grants BIA2011-27217 and BIA2014-59467-R.

References

[1] Yu HS, Mitchell JK. Analysis of cone resistance: review of methods. J Geotech Geoenviron Eng 1998;124(2):140–9.
[2] De Borst R, Vermeer PA. Possibilities and limitations of finite elements for limit analysis. Géotechnique 1984;34(2):199–210.
[3] Arroyo M, Butlanska J, Gens A, Calvetti F, Jamiolkowski M. Cone penetration tests in a virtual calibration chamber. Géotechnique 2011;61(6):525–31.
[4] Ciantia MO, Arroyo M, Butlanska J, Gens A. DEM modelling of cone penetration tests in a double-porosity crushable granular material. Comput Geotech 2016;73:109–27.
[5] Donea J, Huerta A, Ponthot JP, Rodríguez-Ferran A. Arbitrary Lagrangian-Eulerian methods. Encyclopedia of computational mechanics. John Wiley & Sons, Ltd.; 2004. http://dx.doi.org/10.1002/0470091355.ecm009.
[6] van den Berg P, de Borst R, Huétink H. An Eulerean finite element model for penetration in layered soil. Int J Numer Anal Meth Geomech 1996;20 (12):865–86.
[7] Hu Y, Randolph MF. H-adaptive FE analysis of elasto-plastic non-homogeneous soil with large deformation. Comput Geotech 1998;23(1):61–83.
[8] Lu Q, Randolph MF, Hu Y, Bugarski IC. A numerical study of cone penetration in clay. Géotechnique 2004;54(4):257–67.
[9] Zhou H, Randolph MF. Numerical investigation into cycling of full-flow penetrometers in soft clay. Géotechnique 2009;59(10):801–12.
[10] Nazem M, Sheng D, Carter JP. Stress integration and mesh refinement for large deformation in geomechanics. Int J Numer Meth Eng 2006;65(7):1002–27.
[11] Nazem M, Carter JP, Airey DW, Chow SH. Dynamic analysis of a smooth penetrometer free-falling into uniform clay. Géotechnique 2012;62 (10):893–905.
[12] Kardani M, Nazem M, Carter JP, Abbo AJ. Efficiency of high-order elements in large-deformation problems of geomechanics. Int J Geomech 2014;15 (6):1–10.
[13] Dassault Systèmes. Abaqus users manual. Version 6.12; 2012.
[14] Walker J, Yu HS. Adaptive finite element analysis of cone penetration in clay. Acta Geotech 2006;1(1):43–57.
[15] Pucker T, Bienen B, Henke S. CPT based prediction of foundation penetration in siliceous sand. Appl Ocean Res 2013;41:9–18.
[16] Khoa HDV. Numerical simulation of spudcan penetration using coupled Eulerian-Lagrangian method. In: 14th IACMAG Kyoto.
[17] Wang D, Bienen B, Nazem M, Tian Y, Zheng J, Pucker T, et al. Large deformation finite element analyses in geotechnical engineering. Comput Geotech 2015;65:104–14.
[18] Coetzee CJ, Vermeer PA, Basson AH. The modelling of anchors using the material point method. Int J Numer Anal Methods Geomech 2005;29 (9):879–95.
[19] Alonso EE, Zabala F. Progressive failure of Aznalcóllar dam using the material point method. Géotechnique 2011;61(9):795–808.
[20] Sołowski WT, Sloan SW. Evaluation of material point method for use in geotechnics. Int J Numer Anal Meth Geomech 2015;39(7):685–701.
[21] Phuong NTV, van Tol AF, Elkadi ASK, Rohe A. Numerical investigation of pile installation effects in sand using material point method. Comput Geotech 2016;73:58–71.
[22] Ceccato F, Beuth L, Vermeer PA, Simonini P. Two-phase material point method applied to the study of cone penetration. Comput Geotech [in press]. http://dx.doi.org/10.1016/j.compgeo.2016.03.003.
[23] Oñate E, Idelsohn SR, Del Pin F, Aubry R. The particle finite element method: an overview. Int J Comput Methods 2004;1(2):267–307.
[24] Oñate E, Idelsohn SR, Celigueta MA, Rossi R, Marti J, Carbonell JM, et al. Advances in the particle finite element method (PFEM) for solving coupled problems in engineering. In: Particle-Based Methods. Netherlands: Springer; 2011. p. 1–49. http://dx.doi.org/10.1007/978-94-007-0735-1_1.
[25] Rodriguez JM, Carbonell JM, Cante JC, Oliver J. The particle finite element method (PFEM) in thermo-mechanical problems. Int J Numer Methods Eng 2016;56:733–85. http://dx.doi.org/10.1002/nme.5186.
[26] Carbonell JM, Oñate E, Suárez B. Modeling of ground excavation with the particle finite-element method. ASCE J Eng Mech 2010;136(4):455–63.
[27] Carbonell JM, Oñate E, Suárez B. Modelling of tunnelling processes and rock cutting tool wear with the particle finite element method. Comput Mech 2013;52(3):607–29.
[28] Salazar F, Irazábal J, Larese A, Oñate E. Numerical modelling of landslide-generated waves with the particle finite element method (PFEM) and a non-newtonian flow model. Int J Numer Anal Meth Geomech 2016;40(6):809–26. http://dx.doi.org/10.1002/nag.2428.
[29] Zhang X, Krabbenhoft K, Pedroso DM, Lyamin AV, Sheng D, Da Silva MV, et al. Particle finite element analysis of large deformation and granular flow problems. Comput Geotech 2013;54:133–42.
[30] Zhang X, Krabbenhoft K, Sheng D. Particle finite element analysis of the granular column collapse problem. Granular Matter 2014;16(4):609–19.
[31] Zhang X, Krabbenhoft K, Sheng D, Li W. Numerical simulation of a flow-like landslide using the particle finite element method. Comput Mech 2015;55 (1):167–77.
[32] Monforte L, Carbonell JM, Arroyo M, Gens A. Numerical simulation of penetration problems in geotechnical engineering with the particle finite element method (PFEM). In: Oñate E, Bischof M, Owen DRJ, Wriggers P, Zohdi T, Editors. Particles; 2015.
[33] Dadvand P, Rossi R, Oñate E. An object-oriented environment for developing finite element codes for multi-disciplinary applications. Arch Comput Methods Eng 2010;17(3):253–97.
[34] Monforte L, Carbonell JM, Arroyo M, Gens A. Performance of mixed formulations for the particle finite element method in soil mechanics problems [submitted for publication].
[35] Monforte L, Arroyo M, Gens A, Carbonell JM. Explicit finite deformation stress integration of the elasto-plastic constitutive equations. In: 14th IACMAG Kyoto.
[36] Barbosa-Cruz ER. Partial consolidation and breakthrough of shallow foundations in soft soil, PhD thesis. The University of Western Australia; 2007.
[37] Zienkiewicz OC, Taylor RL. The finite element method: solid mechanics, vol. 2. Butterworth-Heinemann; 2000.
[38] Preisig M, Prévost JH. Stabilization procedures in coupled poromechanics problems: a critical assessment. Int J Numer Anal Meth Geomech 2011;35 (11):1207–25.
[39] Dohrmann CR, Bochev PB. A stabilized finite element method for the stokes problem based on polynomial pressure projections. Int J Numer Meth Fluids 2004;46(2):183–201.
[40] Bochev PB, Dohrmann CR, Gunzburger MD. Stabilization of low-order mixed finite elements for the Stokes equations. SIAM J Numer Anal 2006;44 (1):82–101.
[41] Simo JC, Hughes TJR. Computational inelasticity. Springer Science & Business Media; 2006.
[42] Bathe KJ. Finite element procedures. Prentice-Hall; 2006.
[43] Simo JC. Numerical analysis and simulation of plasticity. Handbook Numer. Anal. 1998;6:183–499.
[44] Abbo AJ, Lyamin AV, Sloan SW, Hambleton JP. A C2 continuous approximation to the Mohr-Coulomb yield surface. Int J Solids Struct 2011;48(21):3001–10. http://dx.doi.org/10.1016/j.ijsolstr.2011.06.021.
[45] Armero F, Pérez-Foguet A. On the formulation of closest-point projection algorithms in elastoplasticity-Part I: the variational structure. Int J Numer Meth Eng 2002;53(2):297–329.
[46] Rouainia M, Wood DM. Computational aspects in finite strain plasticity analysis of geotechnical materials. Mech Res Commun 2006;33(2):123–33.
[47] Pérez-Foguet A, Armero F. On the formulation of closest-point projection algorithms in elastoplasticity – Part II: globally convergent schemes. Int J Numer Meth Eng 2002;53(2):331–74.
[48] Sloan SW, Abbo AJ, Sheng D. Refined explicit integration of elastoplastic models with automatic error control. Eng Comput 2001;18(1–2):121–94.
[49] Sheng D, Eigenbrod KD, Wriggers P. Finite element analysis of pile installation using large-slip frictional contact. Comput Geotech 2005;32(1):17–26.
[50] Wriggers P. Finite element algorithms for contact problems. Arch Comput Methods Eng 1995;2(4):1–49.
[51] Wriggers P. Computational contact mechanics. Berlin, Heidelberg: Springer-Verlag; 2006. http://dx.doi.org/10.1007/978-3-540-32609-0.
[52] Rashid MM. Material state remapping in computational solid mechanics. Int J Numer Meth Eng 2002;55(4):431–50.
[53] Farrell PE, Piggott MD, Pain CC, Gorman GJ, Wilson CR. Conservative interpolation between unstructured meshes via supermesh construction. Comput Methods Appl Mech Eng 2009;198(33):2632–42.
[54] Sheng D, Nazem M, Carter JP. Some computational aspects for solving deep penetration problems in geomechanics. Comput Mech 2009;44(4):549–61.
[55] da Silva MV, Krabbenhoft K, Lyamin AV, Sloan SW. Rigid-plastic large-deformation analysis of geotechnical penetration problems. In: Khalili, Oeser, editors. Proceedings of 13th IACMAG conference. Computer methods for geomechanics: frontiers and new applications, vol. 1; 2011. p. 42–7.
[56] Gourvenec SM, Mana DSK. Undrained vertical bearing capacity factors for shallow foundations. Géotech Lett 2011;1(4):101–8.
[57] Wang CX, Carter JP. Deep penetration of strip and circular footings into layered clays. Int J Geomech 2002;2(2):205–32. http://dx.doi.org/10.1061/(ASCE)1532-3641(2002)2:2(205).
[58] Yu L, Liu J, Kong X, Hu Y. Three-dimensional RITSS large displacement finite element method for penetration of foundations into soil. Comput Geotech 2008;35(3):372–82. http://dx.doi.org/10.1016/j.compgeo.2007.08.007.
[59] Qiu G, Henke S, Grabe J. Application of a coupled Eulerian-Lagrangian approach on geomechanical problems involving large deformations. Comput Geotech 2011;38(1):30–9. http://dx.doi.org/10.1016/j.compgeo.2010.09.002.
[60] Einav I, Randolph MF. Combining upper bound and strain path methods for evaluating penetrometer resistance. Int J Numer Meth Eng 2005;63 (14):1991–2016.
[61] Randolph M, Andersen K. Numerical analysis of T-bar penetration in soft clay. Int J Geomech 2006;6(6):411–20.
[62] Lu Q, Hu Y, Randolph MF. FE analysis for T-bar and spherical penetrometers in cohesive soil. In: The tenth international offshore and polar engineering conference. International Society of Offshore and Polar Engineers.
[63] Teh CI, Houlsby GT. An analytical study of the cone penetration test in clay. Géotechnique 1991;41(1):17–34.
[64] van den Berg P. Analysis of soil penetration, Ph.D. thesis. TU Delft; 1994.
[65] Beuth L. Formulation and application of a quasi-static material point method, Ph.D. thesis. University of Sturttgart; 2012. http://dx.doi.org/10.18419/opus-456.